Surface functionalized N-C-TiO_2/C nanocomposites derived from metal-organic framework in water vapour for enhanced photocatalytic H_2 generation

Hussain, Mian Zahid; Yang, Zhuxian; Linden, Bart van der; Huang, Zheng; Jia, Quanli; Cerrato, Erik; Fischer, Roland A.; Kapteijn, Freek; Zhu, Yanqiu; Xia, Yongde

DOI
10.1016/j.jechem.2020.08.048

Publication date
2021

Document Version
Final published version

Published in
Journal of Energy Chemistry

Citation (APA)
Hussain, M. Z., Yang, Z., Linden, B. V. D., Huang, Z., Jia, Q., Cerrato, E., Fischer, R. A., Kapteijn, F., Zhu, Y., & Xia, Y. (2021). Surface functionalized N-C-TiO_2/C nanocomposites derived from metal-organic framework in water vapour for enhanced photocatalytic H_2 generation. *Journal of Energy Chemistry*, *57*, 485-495. https://doi.org/10.1016/j.jechem.2020.08.048

Journal of Energy Chemistry 57 (2021) 485–495

Contents lists available at ScienceDirect

Journal of Energy Chemistry

journal homepage: www.elsevier.com/locate/jechem

http://www.journals.elsevier.com/journal-of-energy-chemistry/

Surface functionalized N-C-TiO_2/C nanocomposites derived from metal-organic framework in water vapour for enhanced photocatalytic H_2 generation

Mian Zahid Hussain [a,b], Zhuxian Yang [a], Bart van der Linden [c], Zheng Huang [a], Quanli Jia [d], Erik Cerrato [e], Roland A. Fischer [b], Freek Kapteijn [c], Yanqiu Zhu [a], Yongde Xia [a,*]

[a] College of Engineering, Mathematics and Physical Sciences, University of Exeter, Exeter EX4 4QF, United Kingdom
[b] Department of Chemistry and Catalysis Research Center, Technical University of Munich, Garching 85748, Germany
[c] Catalysis Engineering, Chemical Engineering Department, Delft University of Technology, van der Maasweg, 9, 2629 HZ Delft, Netherlands
[d] Henan Key Laboratory of High Temperature Functional Ceramics, Zhengzhou University, Zhengzhou 450052, Henan, China
[e] Department of Chemistry, University of Turin, Via P. Giuria, 7, 10125 Turin, Italy

ARTICLE INFO

Article history:
Received 1 July 2020
Revised 18 August 2020
Accepted 23 August 2020
Available online 4 September 2020

Keywords:
Metal-organic framework
TiO_2
Porous carbon
Nanocomposite
Photocatalysis
Hydrogen generation

ABSTRACT

Surface-functionalized nitrogen/carbon co-doped polymorphic TiO_2 phase junction nanoparticles uniformly distributed in porous carbon matrix were synthesized by a simple one-step pyrolysis of titanium based metal–organic framework (MOF), NH_2-MIL-125(Ti) at 700 °C under water vapour atmosphere. Introducing water vapour during the pyrolysis of NH_2-MIL-125(Ti) not only functionalizes the derived porous carbon matrix with carboxyl groups but also forms additional oxygen-rich N like interstitial/intraband states lying above the valence band of TiO_2 along with the self-doped carbon, which further narrows the energy band gaps of polymorphic TiO_2 nanoparticles that enhance photocatalytic charge transfer efficiency. Without co-catalyst, sample N-C-TiO_2/C_{ArW} demonstrates H_2 evolution activity of 426 μmol g_{cat}^{-1} h^{-1}, which remarkably outperforms commercial TiO_2 (P-25) and N-C-TiO_2/C_{Ar} with a 5-fold and 3-fold H_2 generation, respectively. This study clearly shows that water vapour atmosphere during the pyrolysis increases the hydrophilicity of the Ti-MOF derived composites by functionalizing porous carbon matrix with carboxylic groups, as well as enhancing the electrical conductivity and charge transfer efficiency due to the formation of additional localized oxygen-rich N like interstitial/intraband states. This work also demonstrates that by optimizing the anatase–rutile phase composition of the TiO_2 polymorphs, tuning the energy band gaps by N/C co-doping and functionalizing the porous carbon matrix in the N-C-TiO_2/C nanocomposites, the photocatalytic H_2 generation activity can be further enhanced.

1. Introduction

The accelerating industrial growth, ever-increasing energy consumption to run the global economies, together with the simultaneously depleting fossil fuel reserves and the consequential environmental pollution, lead us to explore the alternative low cost and sustainable clean energy sources [1,2]. Enormous efforts have been devoted by academic and industrial researchers to find out the most plausible solutions. In this regard, mimicking the natural photosynthesis process can potentially offer a scientifically practical solution to these persisting problems. Thus, artificial photosynthesis or photocatalysis provides a great promise due to the practical achievability, understandable working mechanisms and the low-cost synthesis of semiconductor materials. The photocatalysis only requires sunlight as energy input and a suitable semiconductor material as a photocatalyst with an appropriate energy band gap. Different semiconducting materials have been extensively explored for water splitting to generate H_2 fuel [3–5]. However, the commercially available semiconducting materials usually have wider energy band gaps and faster surface charge recombination due to the strong coulombic force [1]. Such major scientific challenges must be overcome to achieve stable and high performing visible light photocatalytic materials. The low surface area and agglomeration of particles make the active sites of conventional metal oxides less accessible for catalytic reactions which result in poor photocatalytic performances. Another critical problem of the pure metal oxides based photocatalysts is that a noble metal

* Corresponding author.
E-mail address: Y.Xia@exeter.ac.uk (Y. Xia).

https://doi.org/10.1016/j.jechem.2020.08.048

such as Pt or Au needs to be introduced as a charge mediator, which makes these photocatalysts commercially unaffordable [6]. Hence, the development of new hybrid materials with narrow energy band gaps and high surface area is of utmost importance to find alternative solutions to overcome these challenges.

Due to the natural abundance, low cost and non-toxicity, TiO_2 is one of the most promising semiconductor materials among the available photocatalysts. TiO_2 has three common phase structures: anatase, rutile and brookite [7]. The mixed phases such as anatase and rutile of TiO_2 polymorphs are better photocatalysts than the single phase TiO_2 [8,9]. The energy band gaps (EBGs) of the bulk anatase and rutile phases of TiO_2 are 3.2 and 3.03 eV respectively [10]. With appropriate ratios, these polymorphs can form a phase junction between anatase and rutile phases, which facilitates the spatial separation of photoinduced electrons and holes, resultantly minimizing the charge recombination [1,11,12]. Many studies are available on the formation of phase junction of TiO_2 nanoparticles [1,13–18]. However, the issues of better light absorption, improved interaction between the water molecules and the photocatalyst as well as the accessibility of the active sites are still challenges needed to be addressed. As a result, high surface area semiconducting materials with well-dispersed metal oxide nanoparticles are required for high performing visible light photocatalytic H_2 evolution. Many methods have been tried to increase the specific surface areas and narrow the energy band gaps to make the TiO_2 nanoparticles photoactive under visible light. Different forms of carbon structures such as graphene or graphitic carbon have been introduced into TiO_2 to form composites, but the physical mixing of these two materials does not provide a homogeneous distribution of the metal oxide in carbon with convincing interfacial contacts for better charge transfer [19].

Metal-organic frameworks (MOFs) possess exceptionally high specific surface areas and tunable open pore structures with highly accessible catalytic active sites. MOFs are chemically fabricated coordination polymers with reticular structures that are synthesized by the self-assembly of metal ions or clusters and organic linkers, therefore they usually exhibit highly crystalline porous structures [20]. Some transition metal based MOFs are photoactive and show some photocatalytic activity under visible light irradiation [21,22]. One of the most popular Ti-MOFs, NH_2-MIL-125(Ti) has demonstrated reasonable photocatalytic H_2 activity. Despite having high surface area and accessible metal sites, the poor charge generation and the limitations in electric charge transfer make them less favourable candidates for photocatalysis [4,23,24]. However, in the past few years, MOFs have emerged as excellent precursors or sacrificial templates to derive self-doped metal oxide nanoparticles embedded in functionalized porous carbon structures with inherited high surface area and permanent pores for energy and environmental applications [21,25,26].

In this study, we demonstrate that Ti-MOF, NH_2-MIL-125(Ti) can be an excellent sacrificial template to *in-situ* derive N and C co-doped mixed phase TiO_2 nanoparticles (anatase and rutile) uniformly distributed in a porous carbon matrix which is functionalized with N and/or carboxylic functional groups. The derived N-C-TiO_2/C composites retain the morphologies inherited from the parental NH_2-MIL-125(Ti). This work contributes to the understanding of the effect of the gaseous atmosphere on the carbonization of NH_2-MIL-125(Ti), formation of the N/C self-doped TiO_2 polymorphs and the nature of functionalized porous carbon matrix. For this purpose, the as-synthesized NH_2-MIL-125(Ti) was pyrolyzed at 700 °C under argon atmosphere as well as water vapour to obtain TiO_2/C composites. The use of two different gaseous atmospheres is to investigate the role of oxygen species in the formation of doped TiO_2 nanoparticles as well as the functionalization of the porous carbon matrix. In an argon atmosphere, TiO_2 is doped with substitutional N and C atoms whereas the pyrolysis in a water vapour atmosphere results in formation of oxygen-rich N like interstitial/intraband species and C doping in TiO_2 lattice as well as the –OH/–COOH surface functionalization of carbon matrix due to the presence of oxidative species. These as-prepared nanocomposites were directly used for H_2 generation under UV–Visible light without adding any expensive noble metal as co-catalyst. The best performing sample prepared under water vapour gaseous atmosphere (N-C-TiO_2/C_{ArW}) at 700 °C shows H_2 evolution activity of 426 μmol g_{cat}^{-1} h^{-1}, which is 5-times and 3 times of the commercial TiO_2 (P-25) and the sample prepared in argon atmosphere (N-C-TiO_2/C_{Ar}), respectively. Functionalization of the porous carbon matrix with carboxylic groups as well as the introduction of additional localized oxygen-rich N like interstitial/intraband states can significantly enhance the charge transfer efficiency of MOF derived nanocomposites. This study of MOF derived N/C co-doped TiO_2/C composites demonstrates that the photocatalytic H_2 evolution activity can be enhanced manifold via *in-situ* optimizing the anatase–rutile phase composition of TiO_2 polymorphs, tuning the energy band gaps by controlled anionic doping of nitrogen and carbon species as well as hydrophilic functionalization of the porous carbon matrix.

2. Experimental

2.1. Synthesis of NH_2-MIL-125(Ti)

All the chemicals for the synthesis of NH_2-MIL-125(Ti) were purchased from Sigma-Aldrich and used directly with no further purification. NH_2-MIL-125(Ti) was synthesized following the method reported by Sohail *et al.* with slight modification [22]. For scaled-up synthesis, 44.95 mmol (8.143 g) of 2-aminoterephthalic acid was dissolved in 50 mL dimethylformamide (DMF) and 50 mL methanol (MeOH) solution in a 200 mL screw jar. Then, 11 mmol (3.71 mL) $Ti(OBu)_4$ was slowly added and constantly stirred for 15 min before place it in an oil bath at 130 °C for 40 h. Yellow coloured product was collected by centrifugation followed by washing twice with DMF to remove all the unreacted organic ligand species and then twice with MeOH for solvent exchange. The obtained NH_2-MIL-125(Ti) was dried in air at 70 °C overnight.

2.2. Synthesis of N/C co-doped N-C-TiO_2/C nanocomposites

Nitrogen/carbon co-doped N-C-TiO_2/C nanocomposites were prepared by one-step direct carbonization of precursor NH_2-MIL-125(Ti) at 700 °C under inert atmosphere (Ar) as well as water vapour. For each sample, 1 g of the as-prepared precursor was loaded in an alumina boat and placed at the centre of a flow-through quartz tube sitting in a tube furnace. The heating rate and dwell time of the furnace were 5 °C/min and 2 h, respectively. The flow rate of argon gas was 50 mL/min. The quartz tube was purged for 30 min to make sure that no oxygen is present in the tube before starting the heating process. The sample obtained from carbonization under argon is named as N-C-TiO_2/C_{Ar}. For the second sample, when the tube furnace reached the target temperature during the carbonization process, water vapour was introduced along with the argon gas (50 mL/min passing through a water buffer bottle at room temperature to carry the saturated vapours before entering the tube furnace) for 2 h (only at dwell time). This sample is named as N-C-TiO_2/C_{ArW}. To explore the influence of carbonization temperature, two more samples were obtained at carbonization temperature of 550 and 800 °C in Ar following the same procedure as the preparation of N-C-TiO_2/C_{Ar}. These samples are named as N-C-TiO_2/C_{550Ar} and N-C-TiO_2/C_{800Ar}, respectively. For comparison, the commercially available TiO_2 (P-25), labelled

as TiO_2, is taken as a reference for the photocatalytic H_2 evolution test without further treatment.

2.3. Material characterizations

Powder X-ray diffraction (PXRD) measurements of precursor and their derived composites were performed by *Bragg-Brentano* geometry in a *PANalytical* Empyrean diffractometer equipped with a *PANalytical* PIXcel 1D detector. X-ray diffraction patterns of MOF and derived composites were measured by using Cu K_α radiation (λ_1 = 1.5406 Å, λ_2 = 1.5444 Å, I_2/I_1 = 0.5). K_β radiation was removed with a Ni-filter. The measurement range was fixed between 5° and 90° (2θ) with a step size of 0.040° (2θ) and an acquisition time of 35 s per step. The morphologies of the NH_2-MIL-125(Ti), derived N-C-TiO_2/C composites and TiO_2 were characterized using xT Nova Nanolab 600 FIB coupled with *in-situ* imaging all in one unit. For SEM images, a small amount of powder samples was spread on a carbon tape and sputtered with a thin gold layer of 5 nm to avoid charging of samples. High-resolution TEM images and elemental mapping of the as-prepared composites were carried out by transmission electron microscopy (TEM) (JEM 2100 LeB6 200 kV) equipped with energy dispersive X-ray spectroscopy (EDX). For high-resolution imaging as well as elemental mapping, the samples were dispersed in absolute ethanol under moderate sonication, then pipetted a few drops onto a holey carbon Cu grid followed by drying in air at 70 °C overnight. Thermal stability of the composites and the weight percentage (wt%) of the metal oxide and carbon in nanocomposites were measured using *Mettler Toledo* TGA/STA 409 PC apparatus with a continuous heating ramp of 10 °C/min under synthetic airflow. For TGA measurement, up to 5 mg of each sample was put into an alumina crucible and heated up to 800 °C. To examine the nature of carbon and metal oxide species, the Raman spectra were recorded employing Renishaw inVia Reflex Raman System RL532C, Class 3B in a range from 20 to 2000 cm^{-1} under 1% laser power. Fourier-transform infrared (FTIR) spectra of the samples were recorded in the range of 4000–400 cm^{-1} using a Bruker Optics Tensor-27 FTIR spectrometer. The surface chemical analysis was obtained by the Kratos Axis Ultra DLD spectrometer with a monochromated Al $K\alpha$ X-ray source operating at 168 W (12 mA × 14 kV). Data were collected with pass energies of 160 eV for survey spectra, and 20 eV for high-resolution scans with step sizes of 1 eV and 0.1 eV, respectively. The analysis chamber pressure was maintained at 1×10^{-9} bar. A combination of magnetic immersion and electrostatic lenses (operating in Hybrid mode) was used and acquired over an area approximately 300×700 μm^2. A magnetically confined charge compensation system was used to minimize charging of the sample surface and the take-of angle for the photoelectron analyzer was 90°. Depth profiling experiments were conducted using a 110 μm diameter spot after etching over a 2 × 2 mm area using 1×10^{-6} Torr argon at 4 kV. Data were analyzed using CasaXPS (v2.3.23) after subtraction of a Shirley background and using modified Wagner sensitivity factors as supplied by the manufacturer. To calculate the energy band gaps of TiO_2/C nanocomposites, UV–Vis absorption spectra were acquired by employing a ThermoScientific Evolution 200 spectrophotometer. The specific surface area (SSA) and the pore size distribution (PSD) of the composites were measured by N_2 sorption at 77 K on a *Quantachrome* Autosorb iQ2 ASiQwin apparatus equipped with a micropore port (1×10^{-5} bar) via the conventional volumetric technique. Before the surface area analysis, the samples were degassed at 180 °C for 6 h under vacuum. The pore size distribution was determined using non-local density functional theory (NLDFT) method. Electrochemical Impedance Spectra (EIS) were measured on a CHI660E electrochemical workstation at room temperature. In a classic three electrode electrochemical setup, graphite rod and silver/silver chloride were used as the counter and reference electrodes respectively in an electrolyte of 0.5 M H_2SO_4 solution. A finely polished glassy carbon (GC) electrode (3 mm in diameter) was used as the working electrode, prepared by depositing a 5 μL solution of the sample ink (2 mg photocatalyst dispersed in 1 mL water–ethanol (4:1 v:v) solution with additional 10 μL 5 wt% Nafion solution by ultrasonic bath for 30 min) followed by drying in air overnight. To measure the electron paramagnetic resonance (EPR) spectrum, an X-band CW-EPR Bruker EMX spectrometer equipped with cylindrical cavity operating at 100 kHz field modulation was employed. Using a 1600 W Xenon lamp (Oriel Instruments) equipped with an IR water filter, the effect of UV-Visible light on EPR spectrum was investigated. During the irradiation time, the lamp power was set at 1000 W . This kind of filter offers good coverage with a range of ± 10 nm.

2.4. Photocatalytic hydrogen evolution reaction (HER) measurements

Photocatalytic hydrogen evolution reaction (HER) experiments were carried out using a 500 W Xe/Hg lamp (66983, Newport). It involved custom-made Pyrex-glass reactor, a CP 9001 gas chromatograph (GC, Chrompack) for analysis of the headspace, a KSLA gas pump and the light source. Light intensity was measured with AvaSpec-3648–2-USB2 (Avantes, the Netherlands). The reactor has a total volume of 42.1 mL including the 17.1 mL headspace and 2 mL dilution volume. The reactor is equipped with a water jacket to precisely control the temperature. The light emitted by the Xe/Hg lamp passes through a lens assembly (77330, Newport) (focusing the beam with the spot size of 2.27 cm^2 reaching the reactor window) and an H_2O filter (61945, Newport). The pump is employed to confirm a sufficient mixing of generated gases in the headspace of the reactor and the stainless steel tubes (2.5 mL/min continuous operation). A probe of the headspace is analyzed every 30 min by the GC. In a typical experiment, 25 mg photocatalyst was suspended in 7.5 mL CH_3OH and 17.5 mL H_2O. The suspension was then placed in the reactor and was purged by an argon flow of 30 mL/min for 30 min to deoxygenate the system. The temperature of the reactor was fixed at 30 °C. After completely deoxygenating the reactor, the illumination was applied followed by GC analysis.

The apparent quantum yield (AQY%) of the derived nanocomposites was calculated at 365 nm using the following equation:

$$\mathrm{AQY}_\lambda\ (\%) = \frac{2 \times \text{number of evolved } H_2 \text{ molecules}}{\text{Total number of incident photons}} \times 100\%$$

3. Results and discussion

The powder X-ray diffraction (PXRD) pattern (Fig. S1a in Supplementary data) confirms the formation of highly crystalline NH_2-MIL-125(Ti). The diffraction peaks at 2θ of 6.6°, 9.6° and 11.5° correspond to the simulated XRD pattern of MIL-125(Ti) [22]. The PXRD patterns of the obtained composites N-C-TiO_2/C_{Ar} and N-C-TiO_2/C_{ArW} derived from precursor NH_2-MIL-125(Ti) are shown in Fig. 1(a). The PXRD peaks of sample N-C-TiO_2/C_{Ar} obtained under argon atmosphere appear at 2θ of 25.2° and 27.4° corresponding to the anatase (101) and rutile (110) phases of TiO_2 respectively. However, in sample N-C-TiO_2/C_{ArW}, the main PXRD peaks of anatase and rutile phases of TiO_2 appear at 2θ of 25.4° (101) and 27.4° (110). For comparison, the PXRD pattern of the commercially available TiO_2 (P-25) was also recorded. Several studies have confirmed that the crystallinity and the ratio of anatase/rutile phase junction of TiO_2 play a very important role in higher performance of photocatalytic reactions. Based on the

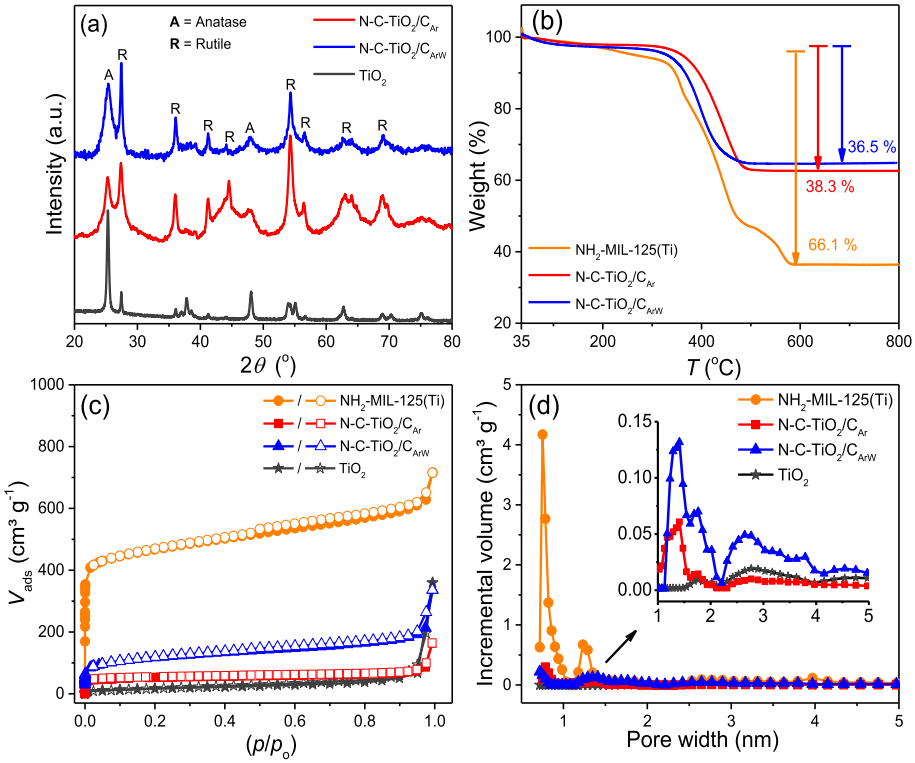

Fig. 1. (a) PXRD patterns, (b) TGA profiles under air, (c) N_2 sorption isotherms and (d) pore size distributions (PSD) of samples NH_2-MIL-125(Ti) (orange), N-C-TiO_2/C_{Ar} (red), N-C-TiO_2/C_{ArW} (blue) and TiO_2 (grey). At 700 °C, both anatase and rutile phases of well-crystalline TiO_2 nanoparticles are present. These polymorphic TiO_2 nanoparticles are embedded in the porous carbon matrix with high BET surface area and tunable pore size distribution.

XRD analysis, the ratio of anatase to rutile phase, as well as the average particle sizes of anatase and rutile phases, can be estimated (Table S1). Introducing water vapour along with argon during pyrolysis of NH_2-MIL-125(Ti) at 700 °C does hardly change the crystal size of the anatase phase, 4.54 nm (for N-C-TiO_2/C_{Ar}) and 5.35 nm (for N-C-TiO_2/C_{ArW}), but the crystal size of the rutile phase changes from 8.28 nm (for N-C-TiO_2/C_{Ar}) to 19.65 nm (for N-C-TiO_2/C_{ArW}). Moreover, a small shift of 0.2° in 2θ is observed in the reflection of the anatase phase of N-C-TiO_2/C_{ArW} [27]. The change in crystallinity, particle size and the shift of reflection position are attributed to the pyrolysis temperature and gaseous atmosphere (water vapour in this case), which play a critical role in determining the crystalline structure, nitrogen and carbon doping, surface functionalization, porosity and weight percentages (wt%) of amorphous carbon in these MOF derived nanocomposites. The commercial TiO_2 (P-25) used as reference contains 84% anatase and 16% rutile phase. Contrary to that, the ratios of anatase to rutile phases of NH_2-MIL-125(Ti) derived TiO_2 polymorphs embedded in porous carbon matrix are estimated to be 45% anatase and 55% rutile phase in N-C-TiO_2/C_{Ar} whereas this ratio is 44% anatase and 56% rutile in N-C-TiO_2/C_{ArW} respectively [28]. Though a minor change, this indicates that the introduction of water vapour during the pyrolysis favours further growth of rutile phase of TiO_2 nanoparticles to relatively larger crystallite sizes and different doping profiles. Moreover, the PXRD patterns presented in Fig. S1(b) suggest that the sample N-C-TiO_2/C_{550Ar} obtained at 550 °C under argon displays poorly developed anatase TiO_2 nanoparticles whereas sample N-C-TiO_2/C_{800Ar} prepared at 800 °C exhibits a mixed anatase and rutile phase of TiO_2 in a composition of 36% and 64%, respectively. Therefore 700 °C is the optimum temperature for the formation of phase junctions between anatase and rutile TiO_2. These nanocomposites were further analyzed by various characterization techniques including TGA, Raman spectroscopy, XPS and BET analysis.

Thermogravimetric analysis (TGA) in the air was carried out to investigate the structural stability and carbon content of the precursor NH_2-MIL-125(Ti) and the derived composites. NH_2-MIL-125(Ti) shows two weight loss events (Fig. 1b). In the range of 50–300 °C, adsorbed moisture, uncoordinated organic linker and residual solvent guest molecules are released with 6 wt% weight loss. The MOF structure stays stable up to 300 °C under airflow. Between 300 and 600 °C the MOF structure collapses causing a weight loss of 60%. All the organic linker (amino-BDC) decomposes and the volatile matter is released, leaving 34 wt% of TiO_2 nanoparticles, in good agreement with the theoretical value (38%) [27]. The TGA profiles of NH_2-MIL-125(Ti) derived N-C-TiO_2/C_{Ar} and N-C-TiO_2/C_{ArW} both show a weight loss of 2 wt% below 200 °C due to the adsorbed moisture. The major weight loss of 38.3% and 36.5% in samples N-C-TiO_2/C_{Ar} and N-C-TiO_2/C_{ArW} occurs between 350 and 600 °C due to the burn-off of the porous carbon matrix. During the high-temperature pyrolysis of the MOF in an argon atmosphere, organic linkers decompose causing a collapse of MOF structure with the release of carbon and nitrogen species and moisture. The introduction of water vapour at the target temperature of 700 °C to produce N-C-TiO_2/C_{ArW} provides an excess of oxygen species which oxidize or gasify the carbon to CO_2 resulting in a further weight loss of 1.8% compared to the sample N-C-TiO_2/C_{Ar}. These MOF-derived N-C-TiO_2/C_{Ar} and N-C-TiO_2/C_{ArW} composites contain 61.7 and 63.5 wt% TiO_2 nanoparticles, respectively, homogeneously embedded in a N/–COOH functionalized porous carbon matrix, which is further confirmed by TEM/EDX and XPS results.

The N_2 sorption isotherms were obtained at 77 K to measure the BET areas and pore size distributions (PSD) of NH_2-MIL-125(Ti) and the derived N-C-TiO_2/C composites. Fig. 1(c) shows that NH_2-MIL-

125(Ti) exhibits type-I isotherms with a high adsorption value below the relative pressure (p/p_0) of 0.1 due to the filling of micropores. The adsorption and desorption isotherms are reversible with negligible hysteresis, signifying the presence of predominantly uniform micropores with a BET area of 1590 $m^2\ g^{-1}$, which is in good agreement with the values reported in the literature [22]. However, the BET surface areas of commercial TiO_2 and NH_2-MIL-125(Ti) derived N-C-TiO_2/C_{Ar} and N-C-TiO_2/C_{ArW} are calculated to be 41, 187 and 378 $m^2\ g^{-1}$, respectively. The derived composites exhibit type-I isotherms with reversible adsorption–desorption branches suggesting the presence of micropores. The small hysteresis in isotherms of N-C-TiO_2/C composites that appeared between relative pressures (p/p_0) of 0.4 and 0.9 is due to the capillary condensation, indicating the formation of a relatively small number of mesopores due to the collapse of the crystalline structure of NH_2-MIL-125(Ti). As summarized in Table 1, the pore volume of the precursor NH_2-MIL-125(Ti) is 0.9 $cm^3\ g^{-1}$, while the pore volumes of the derived N-C-TiO_2/C_{Ar} and N-C-TiO_2/C_{ArW} are 0.13 and 0.33 $cm^3\ g^{-1}$, respectively. Both the BET surface area and pore volume of sample N-C-TiO_2/C_{ArW} are much higher than those of sample N-C-TiO_2/C_{Ar}, which clearly indicates that water vapour during the pyrolysis of precursor NH_2-MIL-125 (Ti) at 700 °C generates more porosity in the resulting composite than only an argon atmosphere, as is expected in carbon gasification [29]. As shown in Fig. 1(d), the pore size distribution (PSD) is calculated by applying a non-local density function theory (NLDFT) model based on the N_2 adsorption data and the main pore size of the samples are also summarized in Table 1. The results suggest that NH_2-MIL-125(Ti) possesses a uniform narrow PSD centred at 0.7 nm. After pyrolysis of NH_2-MIL-125(Ti), a small amount of micropores with a size of 0.7 nm are still retained in the derived N-C-TiO_2/C_{Ar} and N-C-TiO_2/C_{ArW} composites. Moreover, the decomposition of the MOF structure results in a porous carbon matrix with a dominating micropore width of 1.4 nm and a minor mesopore width of 2.6 nm in both derived composites.

Scanning electron microscope (SEM) image of NH_2-MIL-125(Ti) (Fig. S2a) shows tetragonal plates with circular edges. The average size of these tetragonal plates is 800 nm with a thickness of 300 nm [27]. The morphologies of the derived composites N-C-TiO_2/C_{Ar} and N-C-TiO_2/C_{ArW} (Fig. S2b, c) remain largely unchanged, whereas the relative particle sizes are shrunk due to the breaking of coordination bonds between the organic linker and metal cluster during the pyrolysis of NH_2-MIL-125(Ti) precursor at high temperature. Moreover, smaller TiO_2 particles can be observed on the facets of the circular plates in these composites derived at 700 °C [30]. The SEM image of the commercial TiO_2 (P-25) (Fig. S2d) show agglomerated TiO_2 nanoparticles, resulting in less accessible active sites for photocatalytic activity. The NH_2-MIL-125(Ti) derived TiO_2 nanoparticles are, on the other hand, homogeneously distributed in a disk-like porous carbon matrix, resulting in more accessible active sites of TiO_2 with potentially enhanced photocatalytic performance.

To further investigate the morphological and structural transformation upon decomposition of MOF, *in-situ* STEM images were recorded. , As shown in Fig. 2(a), STEM image of a selected NH_2-MIL-125(Ti) crystal show no obvious morphological changes (Fig. 2b)) after *in-situ* heating up to 700 °C under an inert (N_2) gaseous atmosphere. Confirmed by TGA, above 350 °C, the coordination bonds between NH_2-BDC and Ti oxo-cluster start to break and cause a structural transformation followed by the formation of N/C co-doped TiO_2 nanoparticles. At the same time, the NH_2-BDC linker is pyrolytically transformed into an N-functionalized porous carbon matrix [31]. At 700 °C, the diameter of 0.90 μm and thickness of 0.34 μm (Fig. 2a) of selected pristine NH_2-MIL-125(Ti) particle shrunk to 0.64 μm and 0.24 μm (Fig. 2b) respectively, accompanied with the formation of micro/mesoporous carbons. The decomposition of NH_2-MIL-125(Ti) and the morphological changes are in good agreement with TGA results shown in Fig. 1b. The HRTEM images of N-C-TiO_2/C_{Ar} (Fig. 2c and d) and N-C-TiO_2/C_{ArW} (Fig. 2e and f) confirm well crystalline TiO_2 nanoparticles embedded in a porous carbon matrix. The particle sizes are estimated between 10–20 nm distributed homogeneously on the surface and inside the porous carbon matrix without agglomerations. This visual evidence is further supported by the particle sizes of anatase and rutile phases of TiO_2 nanoparticles calculated from PXRD peaks using the Scherrer formula (Table S1). The lattice spacing of these N/C co-doped TiO_2 nanoparticles are estimated to be 0.35 (anatase) and 0.33 nm (rutile) for N-C-TiO_2/C_{Ar} and 0.349 (anatase) and 0.33 nm (rutile) N-C-TiO_2/C_{ArW} respectively [30]. The lattice spacing of the TiO_2 nanoparticles was also confirmed by Bragg's equation using PXRD peaks, which agrees with the HRTEM results. Furthermore, these HRTEM images in Fig. 2(d and f) confirm the formation of anatase/rutile phase junctions at 700 °C.

The advantage of using MOF as a precursor and sacrificial template is that it provides homogeneously distributed self-doped metal oxide nanoparticles in a functionalized porous carbon matrix. To confirm the distribution of the metal oxide in the nitrogen functionalized carbon, elemental mapping was performed using Energy Dispersive X-ray (EDX) Spectroscopy coupled with TEM. It is evident from the representative elemental maps of N-C-TiO_2/C_{Ar} and N-C-TiO_2/C_{ArW} (shown in Fig. 2g and h) respectively that the Ti, O, C and N species are all uniformly distributed throughout the selected area of the sample.

The vibrational modes of the polymorphs of TiO_2 as well as the nature of the porous carbon matrix were confirmed by Raman spectra. As shown in Fig. S3(a), the Raman vibrational modes $E_g(1)$, $B_{1g}(1)$, $A_{1g} + B_{1g}(2)$ and $E_g(3)$ of anatase TiO_2 in sample N-C-TiO_2/C_{Ar} appear at 152, 401.6, 518 and 630 cm^{-1} respectively. These anatase vibrational modes of sample N-C-TiO_2/C_{ArW} are slightly shifted to 152.2, 403, 516 and 628 cm^{-1}, respectively. However, the vibrational modes E_g and A_{1g} of the rutile phase in sample N-C-TiO_2/C_{Ar} (inset in Fig. S3a) are observed at 438 and 598 cm^{-1}, respectively, whereas in sample N-C-TiO_2/C_{ArW}, these modes are slightly shifted to 441 and 586.7 cm^{-1} respectively [32]. The shifts in vibrational modes indicate that the introduction of water vapour during high temperature pyrolysis of NH_2-MIL-125(Ti) not only causes functionalization of the porous carbon matrix but also influences the doping profile of TiO_2 nanoparticles. This observation was further investigated by XPS

Table 1
Textural properties, calculated energy band gaps, H_2 generation activities and apparent quantum yields (AQY%) of studied samples.

Sample	BET surface area ($m^2\ g^{-1}$)	Pore volume ($cm^3\ g^{-1}$)	Pore size (nm)	Energy band gap (eV)	H_2 evolution rate (μmol $g_{cat}^{-1}\ h^{-1}$)	AQY at 365 nm (%)
N-C-TiO_2/C_{Ar}	187	0.13	1.4	3.02	154	0.29
N-C-TiO_2/C_{ArW}	378	0.33	1.4	2.91	426	2.01
Comm. TiO_2 (P-25)	41	0.21	4.7	3.16	82	0.39
NH_2-MIL-125(Ti)	1590	0.90	0.7	2.40	0.5	0.002

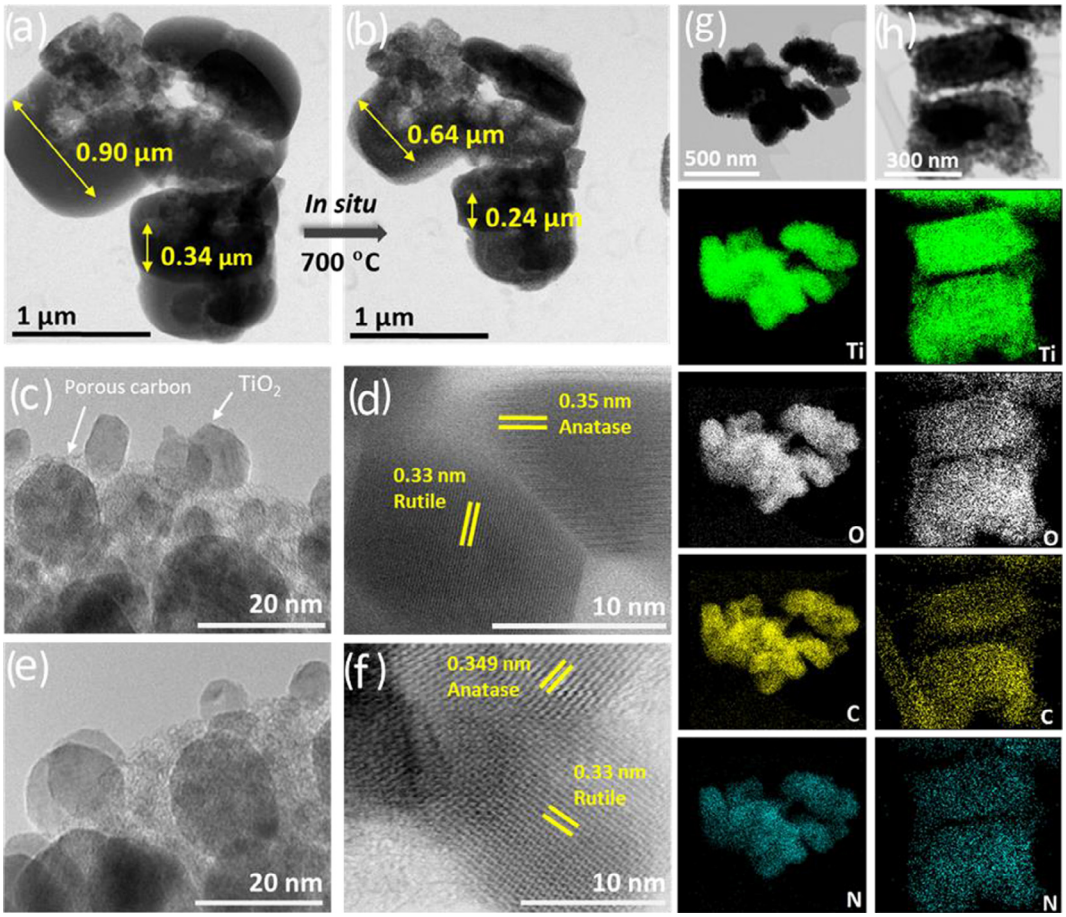

Fig. 2. (a) STEM image of as-prepared NH_2-MIL-125(Ti) and (b) after *in-situ* heating under N_2 gas atmosphere up to 700 °C. The shrinkage of particle size (~30% volume) can be observed with the preserved morphology and porosity. The HRTEM images of (c, d) N-C-TiO_2/C_{Ar} and (e, f) N-C-TiO_2/C_{ArW}. EDX elemental mappings of (g) N-C-TiO_2/C_{Ar} and (h) N-C-TiO_2/C_{ArW} respectively.

spectra. It should be noted that the Raman vibrational modes of pure TiO_2 appear at 144 (Eg(1)), 394 (B_{1g}), 448 (E_g), 516 (A_{1g} + B_{1g}), 613 (A_{1g}) and 638 (E_g(3)) cm^{-1}, respectively [33]. This blue shift of Raman peaks of the MOF derived composites compared to the commercial pure TiO_2 occurs may be due to the N and C doping into the TiO_2 crystal lattice (also confirmed by XPS spectra) as well as the formation of crystal defects upon high-temperature pyrolysis. The presence of N and C atoms may cause a dopant induced strain on the TiO_2 crystal lattices resulting in a shift of the frequencies of the E_g mode [32].

The two signature peaks of D and G bands of amorphous carbon are observed at around 1350 and 1595 cm^{-1} respectively. The G band signifies the bond stretching of sp^2 atoms in hexagonal rings and chains of carbon. This band appears due to the formation of graphitic carbon. However, the D band represents the breathing modes of sp^2 hybridized carbon atoms in hexagonal rings only and appears due to the presence of amorphous carbon [34]. The intensity ratio I_D/I_G of D to G bands is a measure of the defect/disorder content in the crystalline carbon structures. The I_D/I_G ratios of N-C-TiO_2/C_{Ar} and N-C-TiO_2/C_{ArW} are calculated to be 0.91 and 1.0 respectively. The increase in I_D/I_G ratio of these composites reveals that the pyrolysis of NH_2-MIL-125(Ti) in the presence of water vapour produces more disordered carbon with a higher amount of surface functionalities as well as defects. As confirmed by the N_2 sorption isotherms and PSD together with HRTEM, treatment at high temperature in the presence of water vapour a more porous carbon matrix with higher specific surface area and relatively higher amount of micro/mesopores is formed. The Raman spectrum of NH_2-MIL-125(Ti) shown in Fig. S3(a) is in good agreement with literature [27].

The FTIR spectrum of NH_2-MIL-125(Ti) (Fig. S3b) exhibits the typical vibrational bands between 1200 and 1700 cm^{-1} corresponding to the carboxylic acid functional groups of Ti-coordinated MOF structure. The dual stretching absorbance around 3500 cm^{-1} can be assigned to the NH_2 functional groups whereas the sharp absorbance at 769 cm^{-1} to the Ti-O vibrations [27]. For the as-synthesized TiO_2/C samples, the broad FTIR peaks of Ti-O bond stretching modes between the frequencies of 400–800 cm^{-1} (inset in Fig. S3b) were deconvoluted into three distinct absorbances at 731, 630 and 539 cm^{-1} for N-C-TiO_2/C_{Ar} whereas these peaks were observed at 729, 641 and 552 cm^{-1} for N-C-TiO_2/C_{ArW}, respectively [35]. For these NH_2-MIL-125(Ti) derived composites, the appearance of absorbances around 730 cm^{-1} can be assigned to the vibrations of Ti-O-C bonds [36]. Moreover, the shift of positions and their different intensities of Ti-O vibrational modes in N-C-TiO_2/C_{Ar} and N-C-TiO_2/C_{ArW} indicate that the pyrolysis under water vapour influences not only the doping ratios of the N and C species but the localized defect formation in TiO_2 crystal lattices, which results in the modification of energy band gaps [36,37]. The low intensity sharp absorbance at around 1385 cm^{-1} in both derived N-C-TiO_2/C composites can be assigned to the stretching modes of carboxylate groups (O-C = O). A shoulder at 1615 cm^{-1} represents the vibrational mode of O–H. A small but sharp absorbance appearing only in sample N-C-TiO_2/C_{ArW} at 1707 cm^{-1} can be attributed to the C = O bond formed due to the water present during pyrolysis.

To ascertain the chemical state of TiO_2 and the nitrogen and carbon doping in the derived composites, XPS spectra of N-C-TiO_2/C_{Ar} and N-C-TiO_2/C_{ArW} were recorded. The survey spectrum confirms the presence of Ti, O, C and N species in both composites (Fig. S4a). Fig. 3(a) shows that the Ti $2p_{3/2}$ peaks of N-C-TiO_2/C_{Ar} and N-C-TiO_2/C_{ArW} appearing at binding energies of 459.24 and 458.97 eV, respectively, and the Ti $2p_{1/2}$ peak at around 464.8 eV. The Ti $2p_{3/2}$ peak of pure TiO_2 is normally at around 459.3 eV [38]. A negative shift observed in the binding energy of Ti $2p_{3/2}$ depends upon the concentration of N and C doping as well as the formation of oxygen related defects [39]. In the presence of water vapour during pyrolysis, the N can be oxidized to form oxygen-rich N like interstitial states, which may generate new intraband states (energy levels) above the valence band that narrows the energy band gaps [31,38,40]. Consequently, compared to N-C-TiO_2/C_{Ar}, a negative shift of 0.27 eV in the binding energy of the Ti$2p_{3/2}$ peak for sample N-C-TiO_2/C_{ArW} is observed, which may be due to the fact that the introducing oxygen-rich N like interstitial/intraband states can affect and change the surrounding of Ti and result in the formation of Ti-O bond rather than Ti-N bond. The relative atomic concentration (%) of Ti in sample N-C-TiO_2/C_{ArW} is 12.25% compared to N-C-TiO_2/C_{Ar} which is 11.04%. This could be due to a larger carbon loss by gasification during the pyrolysis in a water vapour atmosphere leaving less C in the porous matrix. This is consistent with the obtained TiO_2 content in the two composites from TGA measurements.

Deconvoluting the O 1*s* spectra (Fig. 3b) reveals that two peaks appearing at 530.43 and 532.25 eV with atomic concentrations of 21.59% and 7.4% respectively in sample N-C-TiO_2/C_{Ar}, whereas these peaks shift to 530.17 and 532.0 eV with atomic concentrations of 24.27% and 6.28% respectively in sample N-C-TiO_2/C_{ArW}. The peak at around 530.0 eV is the signature peak of O in TiO_2 lattice. The O 1*s* peaks observed at around 532.0 eV in both samples are attributed to the –OH functional groups present on the TiO_2 and/or carbon surface. Interestingly, a small peak appears at 533.69 eV (with an atomic concentration of 1.22%) in composite N-C-TiO_2/C_{ArW}, which can be assigned to the O = C-O functional groups attached to the carbon matrix [41].

The main binding energy peak of C 1*s* (Fig. 3c) at 284.71 eV in sample N-C-TiO_2/C_{Ar} and 284.56 eV in sample N-C-TiO_2/C_{ArW} correspond to the sp^2 (C = C) bonding in hybridized graphitic carbon as confirmed by Raman spectroscopy. The FWHM of this peak with lower intensity for sample N-C-TiO_2/C_{ArW} compared to that of sample N-C-TiO_2/C_{Ar} indicates the change in chemical state and the number of C = C sp^2 bond due to the pyrolysis in a different gaseous atmosphere. The peak at 285.58 and 285.45 eV in N-C-TiO_2/C_{Ar} and N-C-TiO_2/C_{ArW}, respectively can be assigned to the surface functionalized C-N bond. A broader peak centred at around 286.05 eV is attributed to the C-O bond whereas a small peak at 289.03 eV in both samples represents the O-C = O functional group [41,42].

The doping of N and C atoms into the TiO_2 crystal lattice could be of substitutional or interstitial type. To understand the effect of water vapour on the thermal decomposition of NH_2-MIL-125(Ti) into the derived N-C-TiO_2/C nanocomposites, the N 1*s* XPS spectra (Fig. 3d) can be deconvoluted into several peaks. Valentin *et al.* calculated that the XPS peaks of N-TiO_2 appearing at 396–397 eV, are caused by the substitutional N-dopants in TiO_2 representing the Ti-N bonds, while the peaks at the binding energies higher than

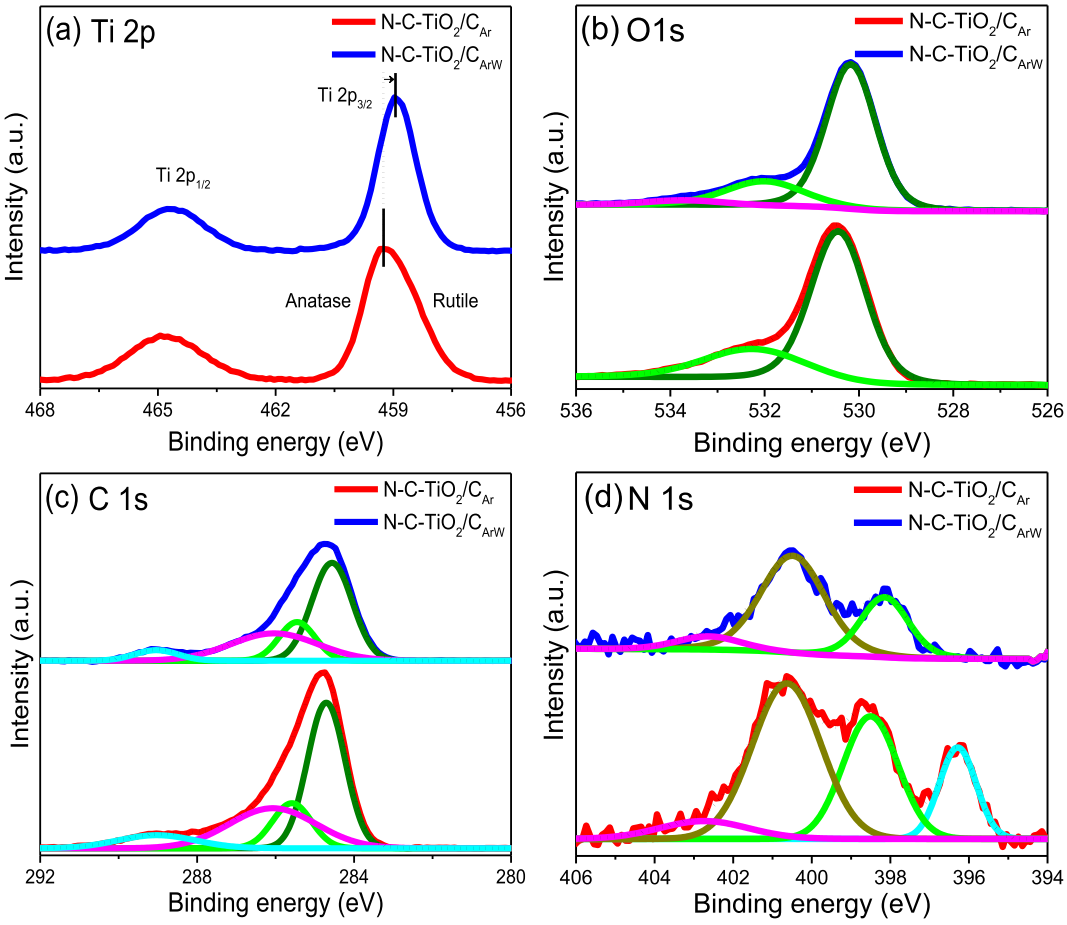

Fig. 3. XPS spectra of (a) Ti 2*p*, (b) O 1*s*, (c) C 1*s* and (d) N 1*s* of composites N-C-TiO_2/C_{Ar} (red) and N-C-TiO_2/C_{ArW} (blue).

400 eV are usually observed in samples with interstitial N sites [37]. This substituted nitrogen replaces the O 2*p* states of the oxygen atoms in TiO_2 with N 1*s* states. Therefore, the peak observed at 396.2 eV with the atomic concentration of 0.42% in sample N-C-TiO_2/C_{Ar} can be assigned to the Ti-N bond between Ti $2p_{3/2}$ and the substituted N-doped atoms originating from the thermal decomposition of the NH_2-BDC linker. Interestingly, this peak is completely absent in sample N-C-TiO_2/C_{ArW}. It can be anticipated in water vapour atmosphere, the formation of Ti-N species is suppressed due to the presence of oxygen-rich water molecules, consequently, the Ti-N species transfers to form Ti-O species in the sample. This results in the complete disappearance of Ti-N peak [37]. In sample N-C-TiO_2/C_{ArW}, the formation of oxygen-rich N like interstitial/intraband states is more favourable. A peak at 400.48 eV can be assigned to the pyrrolic N species with an atomic concentration of 0.34% and 1.23% for N-C-TiO_2/C_{Ar} and N-C-TiO_2/C_{ArW}, respectively. Moreover, a prominent peak observed at 398.59 (1.18% atomic concentration) and 398.14 eV (0.56% atomic concentration) for N-C-TiO_2/C_{Ar} and N-C-TiO_2/C_{ArW}, respectively can be assigned to the pyridine-like N atom [43]. Besides, a small peak at around 402.7 eV may arise from oxidized graphitic N atoms [31].

Obviously, the XPS results of the N 1*s*, O 1*s*, C 1*s* and Ti $2p_{3/2}$ in these composites confirm the substitutional/interstitial types of N/C co-doping in TiO_2 which may result in the narrow energy band gaps and consequently lead to the higher photocatalytic activity under visible light.

To further confirm the chemical states and the elemental distributions of each species, the XPS depth profiling of selected sample N-C-TiO_2/C_{700ArW} was performed. For this purpose, before the measurement, the selected area of the sample was etched using an Ar^+ beam to remove contaminations and adsorbed species from the surface. The average values of Ti 2*p*, O 1*s*, C 1*s* and N 1*s* are quantified as 12.25%, 31.77%, 54.02% and 1.96%, respectively. From etching depth of 20 nm, the Ti, O, N and C content were found to be uniform throughout the etched depth up to 160 nm, confirming the homogenous distribution of these species (Fig. S4b). These results are in complete agreement with EDX elemental mapping (Fig. 2h) of N-C-TiO_2/C_{ArW}.

The optical properties of NH_2-MIL-125(Ti) and the derived N-C-TiO_2/C composites were measured by employing UV–Vis absorption spectroscopy. Fig. S5(a) inset represents the absorption spectra of NH_2-MIL-125(Ti), N-C-TiO_2/C_{Ar} and N-C-TiO_2/C_{ArW} [22]. From the Tauc plots shown in Fig. S5(a), the energy band gaps of NH_2-MIL-125(Ti) and the derived composites N-C-TiO_2/C_{Ar} and N-C-TiO_2/C_{ArW} are estimated to be 2.40, 3.02 and 2.91 eV, respectively. The redshifts in absorption wavelengths (compared to the commercial TiO_2 (P-25)) resulting in the narrowing of energy band gaps are due to the anionic N and C co-doping in the crystal lattice of TiO_2 nanoparticles. From the XPS spectra at lower binding energy, the valence band position (Fig. S5b) of TiO_2 in N-C-TiO_2/C_{Ar} and N-C-TiO_2/C_{ArW} are estimated to be 2.85 and 2.84 eV, respectively. The secondary electron cut off edge shifts from 9.36 eV (N-C-TiO_2/C_{Ar}) to 9.01 eV (N-C-TiO_2/C_{ArW}), indicating the formation of different energy states due to the presence of oxygen species introduced by water vapour at 700 °C. The introduction of water vapour during the pyrolysis of the MOF precursor causes a prominent shift in the absorption band of sample N-C-TiO_2/C_{ArW}. Valentin *et al.* reported that doping TiO_2 with N species in results in a shift of energy band gaps. They claimed that in oxygen deficient conditions substitutional nitrogen (N_s) species were present in TiO_2 crystal lattice above the valance band maxima. However, in oxygen rich conditions, such as in water vapour under high temperature, interstitial nitrogen (N_i) species were more favourable [37]. Table 1 summarizes the estimated energy band gaps of the derived composites. As supported by the XPS analysis of Ti 2*p*, O 1*s* and N 1*s* (Fig. 3a, b and d), the presence of excessive oxygen species from substitutional N species along with oxygen vacancies and formation of defects in TiO_2 results in narrower energy band gaps. The significant difference of 0.11 eV in energy band gap between N-C-TiO_2/C_{Ar} and N-C-TiO_2/C_{ArW} is attributed to the formation of oxygen-rich N like interstitial/intraband species in the TiO_2 crystal lattice.

The photocatalytic H_2 evolution reaction (HER) performance of the NH_2-MIL-125(Ti) derived N-C-TiO_2/C composites were evaluated under UV–Visible light in a methanol aqueous solution without adding any electron mediators such as Pt, Au or Pd. Under the UV–Vis light provided by 500 W Xe/Hg lamp, NH_2-MIL-125(Ti) and the commercial TiO_2 (P-25) were used as references, the HER results are presented in Fig. 4(a). In general, the H_2 evolution increases gradually with the exposure time of the samples to UV–Vis light. After 5 h the studied samples NH_2-MIL-125(Ti), commercial TiO_2 (P-25), N-C-TiO_2/C_{Ar} and N-C-TiO_2/C_{ArW} produced 2.5, 410, 770 and 2130 μmol H_2 g_{cat}^{-1} respectively, indicating that the gaseous atmosphere during pyrolysis plays a critical role in influencing the HER performance of N-C-TiO_2/C composites. The effect of pyrolysis temperature on the HER performance of samples prepared at 550 and 800 °C in argon was also determined (Fig. S6a). Samples N-C-TiO_2/C_{550Ar} and N-C-TiO_2/C_{800Ar} showed an H_2 evolution of 0.5 and 68 μmol g_{cat}^{-1}, respectively, which is much lower than that of sample N-C-TiO_2/C_{Ar} obtained at 700 °C indicating that 700 °C is an optimum temperature for H_2 evolution performance.

Table 1 summarizes the energy band gaps, HER evolution activity and the calculated apparent quantum yield (AQY%) at 365 nm. NH_2-MIL-125(Ti) only exhibits an AQY of 0.002%. Despite narrow energy band gap (2.4 eV) and high specific surface area (1592 m^2 g^{-1}), NH_2-MIL-125(Ti) shows a much lower HER activity and AQY than TiO_2 (P-25) under the same conditions due to the poor charge generation/transfer capacities [44]. The photocatalytic HER performance of composite N-C-TiO_2/C_{Ar} is twice that of pure TiO_2 (P-25), but the sample produced in the presence of water vapour N-C-TiO_2/C_{ArW} outperformed all samples with a photocatalytic HER activity of 426 μmol g_{cal}^{-1} h^{-1}, which is one of the highest photocatalytic H_2 evolution performances amongst co-catalyst free TiO_2-based materials reported in the literature (Table S2). The composite N-C-TiO_2/C_{ArW} also shows AQY value of 2.01%. Generally, the AQY values for these composites are consistent with their H_2 evolution activities. It is worth noting that the AQY is a lower limit of the actual quantum yield because not all the incident photons interact with the photocatalyst to generate photoexcited electrons and holes. The values of AQY% reported in the literature show big variations for a similar type of catalysts due to the different light sources, the geometry of the reactor and experimental conditions. Commonly the incident photons counted by the photodetector are those which strike on the walls of the reactor. The light scattering in solid/liquid heterogeneous medium, as well as small exposed area of reactor window is the significant limiting factors in determining the true quantum yields [45].

The improved H_2 evolution performance of the photocatalysts under UV–Visible light could be explained by the synergistic effect of the mixed crystalline phases with better charge generation, charge transfer and enhanced photocatalytic activity [30]. It is commonly recognized that the synergistic effect of mixed crystalline phases of TiO_2 is determined by many factors such as the energy band gap alignment of anatase and rutile phases, photogeneration of charges and the charge transfer schemes as well as the redox abilities of the photocatalysts [1]. Other important factors that contribute to the enhanced H_2 evolution performance under visible light include the narrow energy band gaps due to the doping by non-metals (C, N or S) and defect formation, a higher number of active sites due to the high surface area of the catalysts and

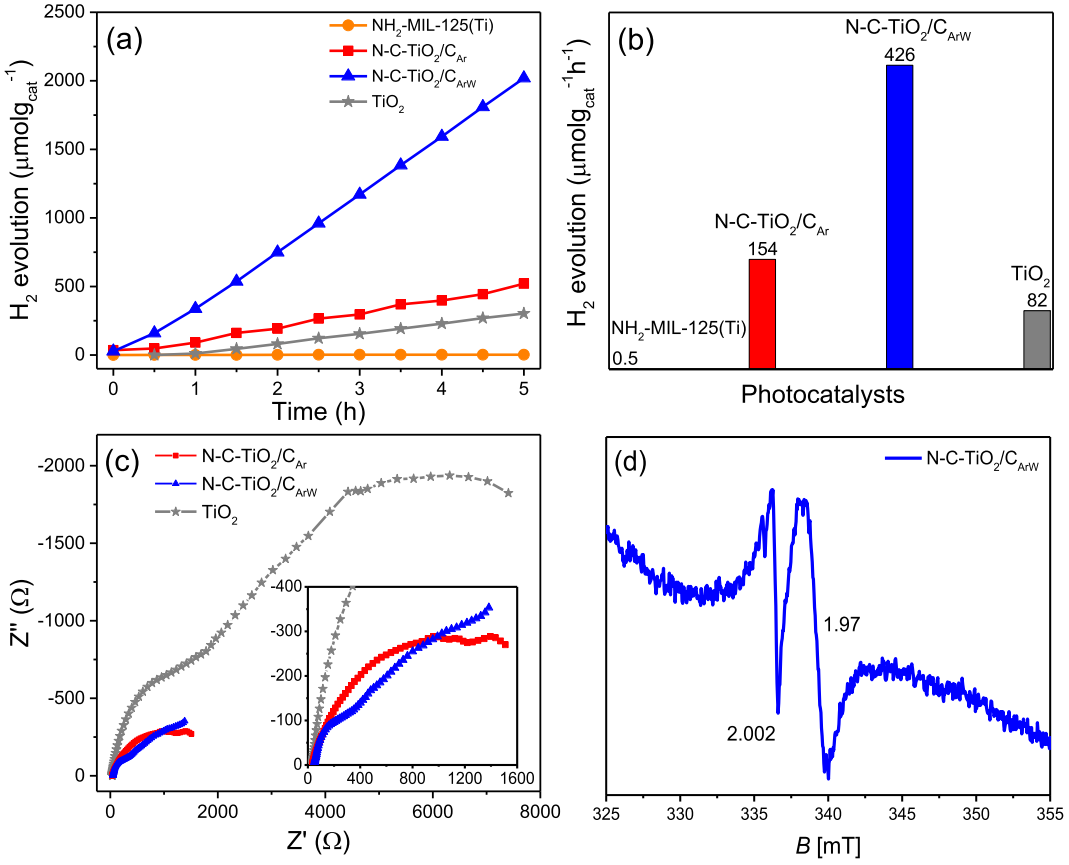

Fig. 4. Photocatalytic H_2 evolution (a) and activity (b) over NH_2-MIL-125(Ti) (orange), TiO_2 (P-25) (grey), N-C-TiO_2/C_{Ar} (red) and N-C-TiO_2/C_{ArW} (blue); (c) EIS Nyquist plots of TiO_2 (P-25), N-C-TiO_2/C_{Ar} and N-C-TiO_2/C_{ArW} under the same potential in 0.5 M H_2SO_4 solution and (d) EPR spectrum of selected N-C-TiO_2/C_{ArW}.

reduced charge recombination due to the presence of co-catalysts [46,47].

The composition of anatase and rutile phases plays a significant role in determining the synergetic effect of TiO_2 polymorphs. Su *et al.* experimentally demonstrated that more than 40% anatase phase and at least 20% rutile phase are necessary for the synergistic effect of TiO_2 photocatalysis. However, the optimum photocatalytic performance should have an anatase/rutile ratio of around 60/40 [8]. Calculated from PXRD peaks, the polymorph of anatase (101) and rutile (110) phase ratio in this study are 45/55 in N-C-TiO_2/C_{Ar} and 44/56 in N-C-TiO_2/C_{ArW} respectively. The samples with the highest photocatalytic H_2 evolution performance are samples that have anatase to rutile phases ratio approximately 1:1, consistent with literature reports [8]. Additionally, the N/C co-doping in anatase/rutile phase junctions of TiO_2 nanoparticles embedded in a porous carbon matrix results in a better charge generation and charge transfer in the photocatalytic H_2 evolution process.

The charge transfer resistance (R_{ct}) was measured by the electrochemical impedance spectroscopy (EIS). The interfacial resistance between the electrode and the electrolyte can be derived from the diameter of the arc or semi-circle in the high frequency region of the Nyquist diagram [48]. It is generally accepted that the smaller the diameter of the arc, the higher the charge transfer efficiency of the material [43]. Fig. 4(c) shows the Nyquist Impedance spectra of TiO_2 (P-25) and MOF derived nanocomposites. The R_{ct} values of N-C-TiO_2/C_{ArW} and N-C-TiO_2/C_{Ar} are 286 and 924 Ω respectively, which are much smaller than that of commercial TiO_2 (P-25) (1744 Ω). This observation confirms that the N/C doped TiO_2 nanoparticles embedded in surface functionalized porous carbon matrix provide much better charge transfer pathways. Interestingly, the R_{ct} value of N-C-TiO_2/C_{ArW} is 3 times smaller than that of the N-C-TiO_2/C_{Ar}, correlating well with their photocatalytic HER results. It is evident that the functionalization of carbon matrix with carboxylate groups (confirmed by FTIR and XPS spectra) not only increases the hydrophilicity of the photocatalysts but also plays an important role in enhancing the electrical conductivity by accelerating the electric charge transfer. As confirmed by Raman spectra, there are plenty of sp^3 defect sites in the NH_2-MIL-125(Ti) derived amorphous porous carbon matrix and the improvement in electrical conductivity can be attributed to the attachment of the electron-withdrawing carboxylate functional groups on sp^3 sites of the carbon matrix [48,49].

The electron paramagnetic resonance (EPR) of the best performing sample N–C-TiO_2/C_{ArW} was measured to investigate the charge generation mechanism upon photoexcitation (Fig. 4d). The spectrum was recorded under UV–Vis light exposing the sample N-C-TiO_2/C_{ArW} for 10 min at temperature 77 K in vacuum condition. A signal appeared at g = 1.97 is due to the presence of Ti^{3+} (g < 2.0) whereas the signal at g = 2.002 confirms the formation of the carbon centred radicals (C•) (whose g value is very close to the free electrons, g_e = 2.0023) [50]. The high intensity signal of C• appears due to the photoexcitation under visible light which indicates that the underlying paramagnetic species may be related to the photocatalytic reaction in carbon doped TiO_2. This signal is usually missing in pure TiO_2 nanoparticles [50–52]. Moreover, due to the presence of oxygen-rich N like interstitial/intraband states in TiO_2 nanoparticles, UV–Vis light causes photoexcitation of electrons from the N centres above the valence band jumping to the conduction bands, and/or transfer to the localized Ti^{3+} states below the conduction band (when irradiation is performed under vac-

uum), consequently, carrying out the water reduction reaction to generate H_2 [47,51].

Based on the above results and discussion, the proposed representative mechanism of photocatalytic H_2 evolution by NH_2-MIL-125(Ti) derived N/C co-doped polymorph TiO_2 nanoparticles embedded in a porous carbon matrix is presented in Fig. 5. Upon UV–Vis light irradiation, electron/hole pairs are generated in anatase and rutile phases of doped TiO_2 nanoparticles. These photogenerated electrons (e^-) jump to the conduction bands and leave the holes (h^+) behind in the valence bands. Deák *et al.* and later Scanlon *et al.* calculated the energy band gap off-set positions in anatase/rutile phase junctions and found that anatase and rutile polymorphs of pure TiO_2 form type-II staggered bands where the valence band of the rutile phase is positioned 0.55 eV above the valence band of the anatase phase. Similarly, the conduction band of the rutile phase also lies 0.35 eV higher than the conduction band of the anatase phase [53]. By computing the branching point energy of the band structures of the anatase and rutile phases, they found that in type-II phase junction with the staggered alignment of the bands, photogenerated electrons migrate and accumulate in the conduction band of the anatase phase while the migrating holes accumulate in the valence band of the rutile phase. This migration of electron and holes reduces the charge recombination, and therefore, the photocatalytic H_2 evolution activity enhances manifold in comparison with the pure anatase and pure rutile TiO_2. Based on the model proposed by Daek and Scanlon, the narrow energy band gap of bulk rutile TiO_2 (3.03 eV) compared to bulk anatase (3.20 eV) TiO_2, may generate more photo-excitons. Because of the band off-set of 0.4 eV (staggered type-II), the anatase phase of TiO_2 exhibits a better electron affinity, favouring the reduction reaction.

In the light of the proposed mechanisms of synergistic photocatalysis, multiple factors play their roles in the NH_2-MIL-125(Ti) derived N-C-TiO_2/C composites simultaneously. The photocatalytic HER results confirm that in N-C-TiO_2/C_{Ar} and N-C-TiO_2/C_{ArW} with anatase–rutile phase junctions, photogenerated electrons of rutile phase migrate to the conduction band of anatase whereas the generated holes transfer to the valence band of the rutile phase. Furthermore, these photogenerated electrons can also transfer to the carbon matrix to minimize the possibilities of charge recombination. The electron-rich anatase phase acts as a photocatalytic active site to reduce the water molecules into H_2 and O_2 species, whereas the oxidation of methanol (MeOH) used as a hole scavenger in the measurement takes place at the valence band of the rutile phase. Besides, the N-functionalized porous carbon matrix with high BET surface area that embeds these uniformly distributed N/C co-doped TiO_2 polymorphs also offer a higher number of active sites which can enhance the accessibility to the photocatalytic reactive sites [54]. More importantly, the doped substitutional oxygen-rich N like interstitial/intraband states and the presence of –OH/–COOH functional groups at the surface of the carbon matrix in N-C-TiO_2/C_{ArW} in comparison with N-C-TiO_2/C_{Ar} increase the adsorption of water molecules. The better interaction of water molecules with the photocatalyst due to these hydrophilic groups results in a 3-fold higher H_2 evolution activity.

The stability of the best performing composite N-C-TiO_2/C_{ArW} was tested for H_2 evolution under UV–Vis light (Fig. S6b) for 22 h without any interruption. Fairly stable performance with only less than 10% decrease in photocatalytic H_2 evolution was observed. It can be concluded that NH_2-MIL-125 (Ti) derived N-C-TiO_2/C nanocomposite by pyrolysis in the presence of water vapour at 700 °C is an excellent photocatalyst for H_2 evolution with good stability under UV–Vis light. This study demonstrates that the photocatalytic hydrogen production performance of these MOF derived nanocomposites can effectively be improved by tuning the energy band gaps of TiO_2 through appropriate non-metal doping, functionalizing the porous carbon matrix with hydrophilic functional groups as well as optimizing the polymorph composition of TiO_2 nanoparticles.

4. Conclusions

We have successfully demonstrated that nitrogen/carbon co-doped (anatase and rutile) TiO_2 phase junction nanoparticles, homogeneously distributed in a N and carboxyl group functionalized porous carbon matrix can be synthesized via a simple one-step pyrolysis of NH_2-MIL-125(Ti) at high temperature in a water vapour containing atmosphere. Various characterization techniques reveal that pyrolysis of NH_2-MIL-125(Ti) in an argon atmosphere at 700 °C results in the N/C co-doped, well-crystalline (anatase and rutile) TiO_2 phase junction with a narrow energy band gap. Introducing water vapour at 700 °C during the pyrolysis of NH_2-MIL-125(Ti) results in the functionalization of the carbon matrix with carboxyl groups as well as the creation of additional localized oxygen-rich N like interstitial/intraband states above the valence band of polymorphic TiO_2 nanoparticles that further narrowed the energy band gap. The derived N-C-TiO_2/C phase junc-

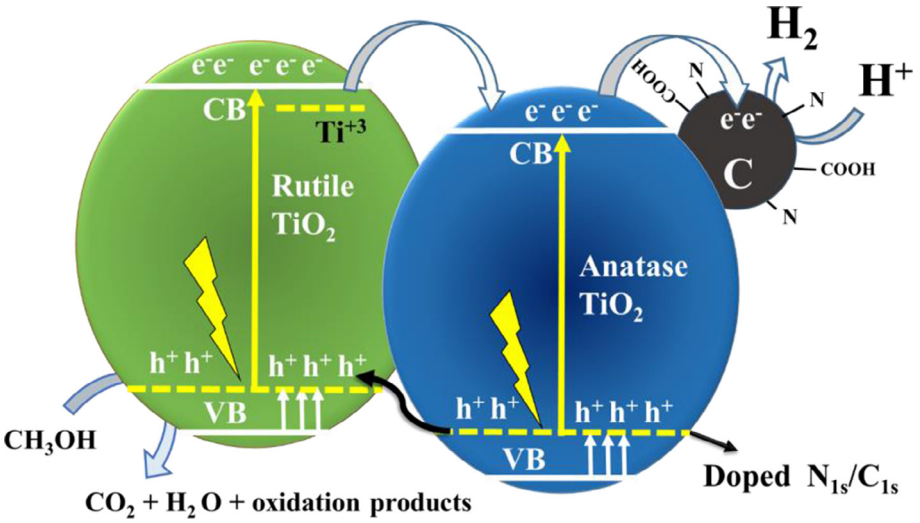

Fig. 5. The proposed representative mechanism of photocatalytic H_2 evolution in NH_2-MIL-125(Ti) derived N-C-TiO_2/C_{ArW}.

tion composites retain the disc-like tetragonal morphologies and textural properties inherited from the NH_2-MIL-125(Ti) precursor. Without loading any noble metal co-catalyst such as Pt, Au, Pd, the sample N–C-TiO_2/C_{ArW} exhibits a photocatalytic HER performance of 426 μmol g_{cat}^{-1} h^{-1}, which outperforms the commercial TiO_2 (P-25) and N-C-TiO_2/C_{Ar} by 5-fold and 3-fold, respectively. It can be concluded that by *in-situ* optimizing the anatase to rutile phase ratio of the N/C codoped TiO_2 polymorphs and functionalizing the porous carbon matrix with the carboxyl group, the photocatalytic H_2 evolution activity under visible light can be effectively enhanced.

Declaration of Competing Interest

The authors declare that they have no known competing financial interests or personal relationships that could have appeared to influence the work reported in this paper.

Acknowledgments

The authors thank EPSRC CDT in Metamaterials at University of Exeter and Leverhulme Trust (RPG-2018-320) for financial support.

Appendix A. Supplementary data

Supplementary data to this article can be found online at https://doi.org/10.1016/j.jechem.2020.08.048.

References

[1] J. Low, J. Yu, M. Jaroniec, S. Wageh, A.A. Al-Ghamdi, Adv. Mater. 29 (2017) 1601694.
[2] J. Fu, J. Yu, C. Jiang, B. Cheng, Adv. Energy Mater. 8 (2017) 1701503.
[3] J. Zhu, P.-Z. Li, W. Guo, Y. Zhao, R. Zou, Coordin Chem. Rev. 359 (2018) 80–101.
[4] H. Wang, Q.-L. Zhu, R. Zou, Q. Xu, Chem 2 (2017) 52–80.
[5] H. Zou, B. He, P. Kuang, J. Yu, K. Fan, Adv. Funct. Mater 28 (2018) 1706917.
[6] P. Ribao, M.J. Rivero, I. Ortiz, Environ. Sci. Pollut. Res. 24 (2017) 12628–12637.
[7] J.-G. Li, T. Ishigaki, X. Sun, J. Phys. Chem. C 111 (2007) 4969–4976.
[8] R. Su, R. Bechstein, L. Sø, R.T. Vang, M. Sillassen, B. Esbjörnsson, A. Palmqvist, F. Besenbacher, J. Phys. Chem. C 115 (2011) 24287–24292.
[9] L. Shi, D. Weng, J. Environ. Sci. 20 (2008) 1263–1267.
[10] A. Kafizas, C.J. Carmalt, I.P. Parkin, Chem. Eur. J. 18 (2012) 13048–13058.
[11] H. Zhang, J. Ming, J. Zhao, Q. Gu, C. Xu, Z. Ding, R. Yuan, Z. Zhang, H. Lin, X. Wang, J. Long, Angew. Chem. Int. Ed. 58 (2019) 7718–7722.
[12] J. Long, H. Chang, Q. Gu, J. Xu, L. Fan, S. Wang, Y. Zhou, W. Wei, L. Huang, X. Wang, P. Liu, W. Huang, Energy Environ. Sci. 7 (2014) 973–977.
[13] Q.L. Xu, L.Y. Zhang, J.G. Yu, S. Wageh, A.A. Al-Ghamdi, M. Jaroniec, Mater. Today 21 (2018) 1042–1063.
[14] F. Xu, W. Xiao, B. Cheng, J. Yu, Int. J. Hydrogen Energy 39 (2014) 15394–15402.
[15] D.O. Scanlon, C.W. Dunnill, J. Buckeridge, S.A. Shevlin, A.J. Logsdail, S.M. Woodley, C.R. Catlow, M.J. Powell, R.G. Palgrave, I.P. Parkin, G.W. Watson, T.W. Keal, P. Sherwood, A. Walsh, A.A. Sokol, Nat. Mater. 12 (2013) 798–801.
[16] L. Fan, J. Long, Q. Gu, H. Huang, H. Lin, X. Wang, J. Catal. 320 (2014) 147–159.
[17] Q. Gu, J. Long, L. Fan, L. Chen, L. Zhao, H. Lin, X. Wang, J. Catal. 303 (2013) 141–155.
[18] Q. Gu, J. Long, H. Zhuang, C. Zhang, Y. Zhou, X. Wang, Phys. Chem. Chem. Phys. 16 (2014) 12521–12534.
[19] K. Qi, B. Cheng, J. Yu, W. Ho, Chinese J. Catal. 38 (2017) 1936–1955.
[20] O.M. Yaghi, M. O'Keeffe, N.W. Ockwig, H.K. Chae, M. Eddaoudi, J. Kim, Nature 423 (2003) 705.
[21] Y.-Z. Chen, R. Zhang, L. Jiao, H.-L. Jiang, Coordin Chem. Rev. 362 (2018) 1–23.
[22] M. Sohail, Y.-N. Yun, E. Lee, S.K. Kim, K. Cho, J.-N. Kim, T.W. Kim, J.-H. Moon, H. Kim, Cryst. Growth Des. 17 (2017) 1208–1213.
[23] W. Wang, X. Xu, W. Zhou, Z. Shao, Adv. Sci. 4 (2017) 1600371.
[24] L. Zeng, X. Guo, C. He, C. Duan, ACS Catal. 6 (2016) 7935–7947.
[25] M.H. Yap, K.L. Fow, G.Z. Chen, Green Energy Environ. 2 (2017) 218–245.
[26] M.Z. Hussain, G.S. Pawar, Z. Huang, A.A. Tahir, R.A. Fischer, Y. Zhu, Y. Xia, Carbon 146 (2019) 348–363.
[27] S. Hu, M. Liu, K. Li, Y. Zuo, A. Zhang, C. Song, G. Zhang, X. Guo, CrystEngComm. 16 (2014) 9645–9650.
[28] X. He, J.W. Ye, Y. Liu, B.Q. Chen, Z.T. Jiang, H.W. Zou, L. Deng, M.J. Tu, Adv. Powder Technol. 21 (2010) 448–451.
[29] J.L.M. Figueiredo, J. A (Eds.), Carbon and coal gasification 105 (1986) 1-655.
[30] Z. Guo, J.K. Cheng, Z. Hu, M. Zhang, Q. Xu, Z. Kang, D. Zhao, RSC Adv. 4 (2014) 34221–34225.
[31] J.R. Pels, F. Kapteijn, J.A. Moulijn, Q. Zhu, K.M. Thomas, Carbon 33 (1995) 1641–1653.
[32] W.F. Zhang, Y.L. He, M.S. Zhang, Z. Yin, Q. Chen, J. Phys. D 33 (2000) 912.
[33] O. Frank, M. Zukalova, B. Laskova, J. Kürti, J. Koltai, L. Kavan, Phys. Chem. Chem. Phys. 14 (2012) 14567–14572.
[34] P.K. Chu, L. Li, Mater. Chem. Phys. 96 (2006) 253–277.
[35] T.C. Jagadale, S.P. Takale, R.S. Sonawane, H.M. Joshi, S.I. Patil, B.B. Kale, S.B. Ogale, J. Phys. Chem. C 112 (2008) 14595–14602.
[36] B. Qiu, Y. Zhou, Y. Ma, X. Yang, W. Sheng, M. Xing, J. Zhang, Sci. Rep. 5 (2015) 8591.
[37] C. Di Valentin, E. Finazzi, G. Pacchioni, A. Selloni, S. Livraghi, M.C. Paganini, E. Giamello, Chem. Phys. 339 (2007) 44–56.
[38] N.C. Saha, H.G. Tompkins, J. Appl. Phys. 72 (1992) 3072–3079.
[39] R. Asahi, T. Morikawa, T. Ohwaki, K. Aoki, Y. Taga, Science 293 (2001) 269–271.
[40] F. Kapteijn, J.A. Moulijn, S. Matzner, H.P. Boehm, Carbon 37 (1999) 1143–1150.
[41] P. Iamprasertkun, A. Krittayavathananon, M. Sawangphruk, Carbon 102 (2016) 455–461.
[42] M.Z. Hussain, A. Schneemann, R.A. Fischer, Y. Zhu, Y. Xia, ACS Appl. Energy Mater. 1 (2018) 4695–4707.
[43] Z. Huang, Z. Yang, M.Z. Hussain, B. Chen, Q. Jia, Y. Zhu, Y. Xia, Electrochim. Acta 330 (2020) 135335.
[44] M.A. Nasalevich, C.H. Hendon, J.G. Santaclara, K. Svane, B. van der Linden, S.L. Veber, M.V. Fedin, A.J. Houtepen, M.A. van der Veen, F. Kapteijn, A. Walsh, J. Gascon, Sci. Rep. 6 (2016) 23676.
[45] N. Serpone, J. Photochem. Photobiol. A 104 (1997) 1–12.
[46] Q. Wang, T. Hisatomi, S.S.K. Ma, Y. Li, K. Domen, Chem. Mater. 26 (2014) 4144–4150.
[47] G. Barolo, S. Livraghi, M. Chiesa, M.C. Paganini, E. Giamello, J. Phys. Chem. C 116 (2012) 20887–20894.
[48] J. Ângelo, P. Magalhães, L. Andrade, A. Mendes, Appl. Surf. Sci. 387 (2016) 183–189.
[49] V.N. Palakollu, R. Karpoormath, Synth. Met. 245 (2018) 87–95.
[50] A.A. Minnekhanov, D.M. Deygen, E.A. Konstantinova, A.S. Vorontsov, P.K. Kashkarov, Nanoscale Res. Lett. 7 (2012) 333.
[51] A. Naldoni, M. Altomare, G. Zoppellaro, N. Liu, Š. Kment, R. Zbořil, P. Schmuki, ACS Catal. 9 (2019) 345–364.
[52] G. Liu, C. Han, M. Pelaez, D. Zhu, S. Liao, V. Likodimos, N. Ioannidis, A.G. Kontos, P. Falaras, P.S.M. Dunlop, J.A. Byrne, D.D. Dionysiou, Nanotechnology 23 (2012) 294003.
[53] P. Deák, B. Aradi, T. Frauenheim, J. Phys. Chem. C 115 (2011) 3443–3446.
[54] S.Y. Han, D.L. Pan, H. Chen, X.B. Bu, Y.X. Gao, H. Gao, Y. Tian, G.S. Li, G. Wang, S. L. Cao, C.Q. Wan, G.C. Guo, Angew. Chem. Int. Ed. 57 (2018) 9864–9869.